POLITECNICO DI TORINO
Repository ISTITUZIONALE

Investigation of Amperometric Sensing Mechanism in Gold-C60-Gold Molecular Dot

(Article begins on next page)

29 November 2022

Investigation of Amperometric Sensing Mechanism in Gold–C$_{60}$–Gold Molecular Dot

Fabrizio Mo, *Graduate Student Member, IEEE*, Yuri Ardesi, *Member, IEEE*,
Massimo Ruo Roch, Mariagrazia Graziano, and Gianluca Piccinini

Abstract—We investigate through simulations the gold–C$_{60}$–gold molecular junction as a novel single-molecule amperometric gas sensor. We find it promising for NO and NO$_2$ detection in air and at room temperature, with current variations of the order of the microampere, and presenting the potential capability of achieving the single-molecule sensitivity along with selectivity in the presence of common atmospheric gases. Furthermore, and for the first time, we investigate the current modulation mechanism due to target–sensor intermolecular interactions, providing theoretical insights into the functioning and exclusive properties of this novel device. In particular, we show and motivate the peculiar voltage-dependent response of the sensor that we relate to the distinctive mechanism of transport modulation occurring in the presence of a specific target. Finally, we discuss sensing reliability in air and the effects of probable fabrication process variability on sensing performance. Our results motivate future works on molecular dot-based chemical sensors in terms of the sensor–target exclusive interactions and detection principles, oriented to device-level engineering to find optimal operating conditions.

Index Terms— Amperometric detection, C$_4$H$_{10}$, C$_{60}$, CH$_4$, CO, CO$_2$, dot, electronics, fullerene, gas, gold, junction, molecular, nanogap, NH$_3$, nitric oxide (NO), NO$_2$, quantum, sensor, single-molecule.
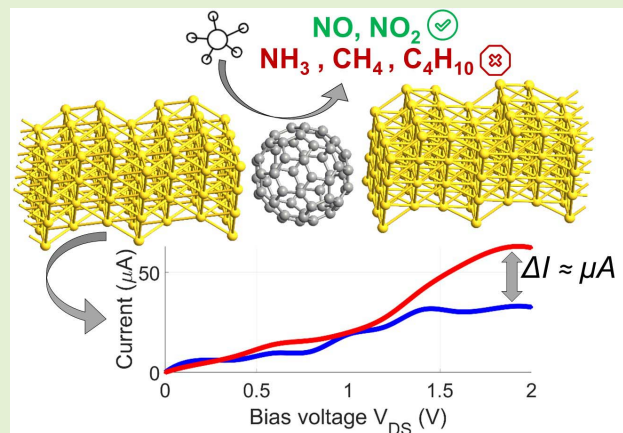
I. INTRODUCTION

A IR pollution is gaining global attention as a cause of climate change and a risk to human health by provoking severe diseases [1], [2]. The current state-of-the-art gas measurement trend is toward nanostructured metal oxide (MOX) chemiresistive sensors, thanks to their high sensitivity, fast response/recovery time, high stability and crystallinity, direct electronic interface, and low fabrication cost [3], [4]. Among them, miniaturized sensors, like nanowires, are promising because of their superior surface-to-volume ratio. Nevertheless, such devices still lack selectivity [3], [4].

At the same time, single-entity and single-molecule detection has been recently achieved as the ultimate detection limit [5]. Such sensors are promising because of their intrinsic high sensitivity, potential selectivity, and calibration-free features, likely constituting the next-generation sensors toward miniaturization and superior performance. These kinds of analytical devices present peculiar properties that make them extremely interesting objects of study: (i) by detecting a single molecule, the sensor is intrinsically calibration-free; (ii) the signal-to-noise ratio does not decrease with decreasing target concentrations; and (iii) the sensor, despite to ensemble entity detection, can differentiate between rare events caused by target chemical species and noise [6], [7].

In this scenario, we investigate through atomistic simulations the gold–C$_{60}$–gold molecular junction (Au–C$_{60}$) as a novel single-molecule gas sensor. In the present work, with a "single-molecule sensor," we intend that both the targets are supposed to be a single molecule and the active portion of the sensor is constituted by a single molecule (namely C$_{60}$).

We concentrate on common atmospheric toxicant and pollutant detection: NO, NO$_2$, NH$_3$, CH$_4$, C$_4$H$_{10}$, along with the most common atmospheric components [1]: Ar, N$_2$, O$_2$, H$_2$O, CO, CO$_2$, to study the sensor selectivity in air. In addition, we consider two possible effects of process variations (namely the C$_{60}$-to-contact distance and the C$_{60}$ orientation) on the sensing mechanism, to understand whether realistic modifications of the sensor structure can compromise the sensing. From our results, the sensor can selectively detect NO and NO$_2$ in air and at room temperature, also in the case of process variation modifications of the sensor structure, thus motivating future research studies in molecular dots as single-molecule sensors.

II. METHODOLOGY AND THEORETICAL CONSIDERATIONS

A. Device Structure

We choose the C$_{60}$ buckminsterfullerene as molecular channel since it is widely discussed in literature, stable at room temperature, simple to synthesize, and its sensing capabilities were already demonstrated [8], [9], [10], [11]. Furthermore, we select gold as the electrode material since it is an inert noble metal and it presents good chemical properties to create molecular break junctions at room temperature [12], [13]. Also, it permits to address a realistic device structure, since in fabrication processes, a gold nanogap can be created by electromigration, by a crack-defined break junction or by a mechanically controllable break junction [13], [14], [15], [16], [17]. Then, we assume C$_{60}$ is deposited in the gap [13], and the two gold face-centered cubic (FCC) (111) sides constitute the source (S) and drain (D) contacts. Fig. 1(a) shows the Au–C$_{60}$ geometry. We consider a gold nanogap of dimension 11.27 Å, and we assume an Au–C bond length of 2.4 Å, with two C$_{60}$ hexagons centered on a gold vacancy in the first gold layer and on a gold atom in the second layer, as in Fig. 1(b). This fullerene chemisorption orientation w.r.t. to Au FCC (111) surfaces is proved to be the most stable and probable one, both theoretically and experimentally [18], [19]. In Section III-H, we consider C$_{60}$ rotated w.r.t. the electrodes, as in Fig. 1(c).

To investigate the Au–C$_{60}$ sensing capabilities, we place the target gas molecules above C$_{60}$, centered w.r.t. S and D, at a distance between 2.2 and 2.5 Å, depending on the specific molecule [see Fig. 1(d)]. In this way, we assure a partial overlap of the target van der Waals radius, that is, a measure of the molecule space occupancy—with that of fullerene [see Fig. 1(e)], meaning that strong intermolecular interactions surely occur.

To test the sensor reliability, we additionally consider the case in which the targets interact with the lateral portions of the fullerene, close to Au surfaces. Whereas, thanks to gold poor reactivity, and by considering that gold electrodes can be passivated by depositing suitable passivation materials, we do not address the case in which targets exclusively interact with gold electrodes instead of the active portion of the sensor, that is, the fullerene.
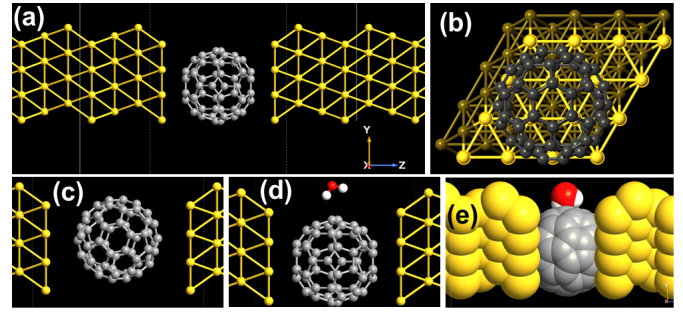

Fig. 1. Elements: yellow is gold, gray is carbon, red is oxygen, white is hydrogen. (a) Au–C$_{60}$ molecular dot. (b) Detail of the geometry—the bright gold layer is the first one. (c) Geometry with rotated C$_{60}$ [less stable than (a)]. (d) Example of sensing geometry with a water molecule placed at 2.21 Å from the C$_{60}$. (e) Same of (d) with van der Waals radii.

B. Theoretical Background

The sensor we address in this work relies on the following principle. In an inert environment, a current I_{DS} flows in the Au–C$_{60}$ dot if a voltage V_{DS} is applied. When a gas molecule is close to the C$_{60}$ channel, we expect an I_{DS} modulation because of the intermolecular interactions that can enhance or counteract the S to D electron transmission (i.e., tunneling). The crucial quantities to be modeled and calculated are thus: 1) the electronic structure of the device; 2) the S to D electron transmittivity and current; and 3) the intermolecular interactions between the channel and the gas molecule.

1) To understand the Au–C$_{60}$ dot electronic states, we first consider the isolated C$_{60}$ and then the effect of contacts. The isolated C$_{60}$ presents discrete energy levels, that is, discrete eigenvalue spectrum, as solution of the steady-state Schrödinger's equation for the C$_{60}$ Hamiltonian operator: $H_{C_{60}}\psi_n = E_n\psi_n$. Because of the time–energy uncertainty relation, since no uncertainty exist on discrete energy eigenvalues, the state lifetimes are infinite

$$\Delta t \Delta E \sim h \Rightarrow \Delta t \to \infty, \quad \text{when } \Delta E = 0 \tag{1}$$

where h is Planck's constant. When C$_{60}$ creates chemical bonds with the S and D electrodes, the total Hamiltonian becomes

$$H = \begin{bmatrix} H_S & H_{S,C_{60}} & 0 \\ H_{C_{60},S} & H_{C_{60}} & H_{C_{60},D} \\ 0 & H_{D,C_{60}} & H_D \end{bmatrix} \tag{2}$$

where no interaction is supposed between S and D (the relative blocks are zero). The coupling Hamiltonians $H_{S/D,C_{60}}$, $H_{C_{60},S/D}$ generate a contact-C$_{60}$ state mixing with the effect of (i) broadening the discrete C$_{60}$ energy levels and (ii) shift them through a mechanism that involves electron wave function redistribution in the total system [20]. The situation is depicted in Fig. 2(a) and (b)—the blue arrows highlight the effects (i) and (ii). The broadening (i) has the effect of introducing an energy uncertainty on the C$_{60}$ energy levels $\Delta E = \gamma$, where γ indicates the amount of broadening of the original level. From (1), with $\Delta t = \tau$, the state lifetime
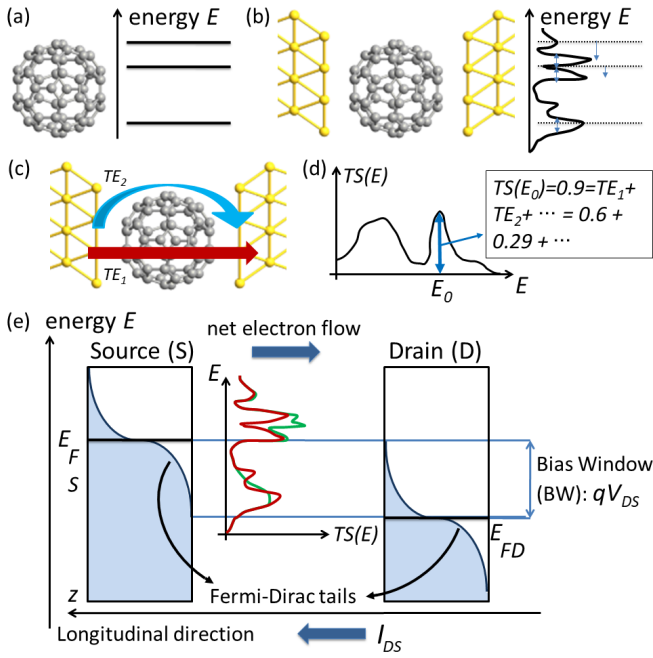
Fig. 2. (a) Isolated C_{60} discrete energy spectrum. (b) Contacted C_{60} continuous energy spectrum. (c) Sketch of different TEs. (d) Example of a TS peak and relative TEs. (e) Principle of operation of the proposed sensor.

in the contacted C_{60} becomes a finite quantity: $\tau \sim h/\gamma$. The physical interpretation is that electrons can escape from C_{60} to go into the contacts and vice versa (electrons freely move between C_{60} and contacts, thanks to chemical bond formation). The greater the broadening γ, that is, the S/D-C_{60} coupling, the lower is the lifetime τ [20].

2) Among the possible electron states, the ones that contribute to conduction are those in between the S Fermi level E_{FS} and the D one E_{FD}, that is, within the so-called bias window (BW). The two contact Fermi–Dirac's distributions $f(E, E_{FS})$ and $f(E, E_{FD})$ account for the occupation probability at any temperature. The quantum nature of the electronic transport is considered through the so-called transmission spectrum $TS(E)$ that provides the total S to D transmission probability for each electron energy E. We use the purely quantum mechanical nonequilibrium Green's function (NEGF) theory to calculate $TS(E)$. This method has the advantage of accurately accounting for all the quantum features of the system under analysis, with maximum generality under all operating conditions [20]. It can be shown that, with the NEGF approach, $TS(E)$ depends on $H_{C_{60}}$, $H_{S/D,C_{60}}$, and $H_{C_{60},S/D}$—details are in [21] and [20]. Depending on the nature of C_{60}-S/D coupling, the transport can be shown to be mainly coherent, in the case of strong coupling (large γ), or mainly incoherent, in the case of weak coupling (small γ). Indeed, if τ is much shorter than the characteristic times of incoherent processes, the electron transmission from S to D will be unaffected by incoherent processes, while, if τ is much longer than the incoherent process characteristic times, incoherent processes have a main role in the electronic transport [20]. Since in our case, C_{60} creates covalent bonds with S and D, as we will discuss in Section III-H, the molecular dot is in the strong coupling regime and the dominant transport mechanism is ballistic transport [21], [22]—we briefly address this point

in Section III-A. The current can be evaluated from $TS(E)$ through Landauer's formula [20]

$$I_{DS} = \frac{2q}{h} \int_{-\infty}^{+\infty} TS(E) \left[f(E, E_{FS}) - f(E, E_{FD}) \right] dE \quad (3)$$

where q is the elementary charge. We then characterize the sensor response to targets in terms of absolute and percentage current deviations, defined as

$$\Delta I_{DS} = I_{DS,gas} - I_{DS,0}$$
$$\Delta I_{DS\%} = \left[\left(I_{DS,gas} - I_{DS,0} \right) / I_{DS,0} \right] \cdot 100 \quad (4)$$

where $I_{DS,0}$ is the Au–C_{60} current and $I_{DS,gas}$ is the Au–C_{60} current in the presence of a specific gas molecule.

3) According to the well-established London's quantum mechanical treatment of intermolecular forces, the effect of a target molecule on the sensor C_{60} channel is to add an electrostatic perturbation to the resultant of the C_{60} atomic forces [23]. In other words, a gas molecule nearby C_{60} perturbs its Hamiltonian $H_{C_{60}}$ by adding an extra potential energy term [23]. Since TS depends on $H_{C_{60}}$, the effect of a target is to modify the sensor $TS(E)$ in (3) and thus the current I_{DS}. To calculate intermolecular interactions, several approaches are possible, from perturbative ones to supermolecular ones [24]. We use the latter approach since a large number of atoms in the Au–C_{60} dot makes perturbational approaches computationally unfeasible [24]. In particular, we use the extended Hückel theory (EHT) method to calculate the device electron states and electronic configuration (refer to Section II-H) and the intermolecular forces are accounted for in this operation. Since van der Waals interactions depend on the relative orientations of the two molecules, we consider different target orientations in our analyses.

C. Transmission Eigenstates

In order to analyze how the targets modify TS, we analyze the so-called transmission eigenstates (TEs) that we now introduce. The effect of contacting C_{60} is to produce, at each energy E, an electron orbital or wave function mixing between the C_{60} states and the contact ones (state hybridization). This is represented by the coupling terms in the system Hamiltonian in (2). Furthermore, as a consequence of level broadening, at each energy E, several broadened energy levels can superimpose, producing the final electron state at that energy E. An electron at energy E can thus be transmitted from S to D through one of the states composing the final state with energy E. In other words, electrons can be transmitted through one orbital or another at the same energy E, by following, therefore, different space paths. The situation is depicted in Fig. 2(c)—blue and red paths. Formally, such different space paths are called TEs, since they are the solutions to an eigenvalue problem for the quantum mechanical transmission operator [21]. It is possible to plot the TEs in space as surfaces of iso-probability of transmission, and we make use of this representation to characterize the Au–C_{60} sensor in Section III. The TEs provide information about where the transmission occurs in space. This information is not included in $TS(E)$, which provides only the total transmission probability for that energy E, through all the possible TEs. Furthermore, since

the TEs are eigenstates, a solution to an eigenvalue problem, they are associated with eigenvalues that have the physical meaning of transmission coefficients, normalized to 1. The transmittivity value of a specific TS peak at $E = E_0$ is the sum of all the transmission coefficients corresponding to all the TEs composing the specific $TS(E_0)$, indeed superposition holds, as aforementioned. Since there is a univocal correspondence between a TE and its transmission coefficient, we call the transmission coefficients $\text{TE}_1, \text{TE}_2, \ldots, \text{TE}_m, \ldots$ and we express $TS(E_0)$ as their sum, as depicted in Fig. 2(d)

$$TS(E = E_0) = \sum_m \text{TE}_m = \text{TE}_1 + \text{TE}_2 + \cdots . \quad (5)$$

In this work, we find that only one or two TEs compose the great majority of a $TS(E_0)$ peak, and thus, by analyzing them, we get an explanation of how the targets modify the TS at a given energy E_0.

D. Additional Analysis Instruments

To characterize the sensors, we additionally use the following two quantities.

1) *Molecular projected self-consistent Hamiltonian (MPSH):* It is a real space projection of the (self-consistently calculated) Hamiltonian. It corresponds to electron orbitals in space, that is, iso-probability surfaces (electron probability density of position).

2) *Projected density of states (PDOS):* It is the density of states of a set of atoms of the device, that is, projected onto the set of atoms.

3) *Mulliken population:* It is equivalent to the number of electrons that, on average, are belonging to an atomic site. When greater/lesser than the element electron number, the atom is negatively/positively charged. Since, in this work, we find that only the valence electron populations are modified by target presence, we refer the results to valence shells electron population only.

E. Conductance and Current Modulation

To highlight how TS variations affect I_{DS}, we rewrite (3) at zero kelvin and then we generalize the concepts at room temperature. At zero kelvin, the Fermi functions are step functions and (3) becomes

$$I_{DS} = \frac{2q}{h} \int_{E_{FD}}^{E_{FS}} TS \, dE = \frac{2q^2}{h} \int_0^{V_{DS}} TS \, dV \simeq G V_{DS} \quad (6)$$

where $E_{FD} = E_{FS} - q V_{DS}$ and we used the change of variable $E = -qV$ and the convention $E_{FS} = -q V_S = 0$ (gnd). The quantity $(2q^2/h)$, usually called quantum conductance [20], has the dimensions of conductance. The latter equality strictly holds only in linear regime—constant TS—nevertheless, it clarifies that the conductance G is proportional to the TS integral over the BW, that is, between E_{FD} and E_{FS}. At greater temperatures, the effect of the Fermi functions is to enlarge the integration domain, from E below E_{FD} to E above E_{FS}, through the Fermi functions "tails," as depicted in Fig. 2(e). For E far below or far above the BW range of energies, the Fermi function difference in (3) is close to zero,

leading to negligible I_{DS} for any TS value. Whereas for E around the BW, the Fermi function difference in (3) is close to unity, meaning that, in general, G and I_{DS} depend on the TS integral in a range of E around the BW.

In this article, we show that target molecules have the capability to significantly modify $TS(E)$ for some E. Fig. 2(e) represents this principle, where the green and red $TS(E)$ curves are the sensor TS with and without the target. Interestingly, as discussed above, $TS(E)$ modifications affect G and I_{DS} only if they are around the BW. Therefore, the sensor response, in terms of G and I_{DS} modulation, depends on the applied V_{DS}, leading to a peculiar voltage-dependent response, as we discuss in Section III-E.

F. Effect of V_{DS} on TS

In general, TS depends also on the applied bias [20]. Indeed, similar to what happens with targets, V_{DS} modifies the potential energy in the system Hamiltonian, and consequently TS: $TS(E, V_{DS})$. Nevertheless, crucial importance has the equilibrium TS: at small bias, TS can be approximated with the equilibrium one [20].

G. Figure of Merit

The effect of a target is to modify TS. We call $TS_0(E)$ the TS of the sensor only, and $TS_{gas}(E)$ the TS of the sensor in the presence of a target. Since Section II-E shows that G and I_{DS} depend on the energy integral of TS, we define the following figure of merit

$$\Delta \int TS = \int_{E_{FD}}^{E_{FS}} TS_{gas}(E) dE - \int_{E_{FD}}^{E_{FS}} TS_0(E) \, dE \quad (7)$$

that multiplied by $(2q/h)$ provides a zero kelvin approximation of the expected current variation because of the presence of the target. To rapidly estimate whether an I_{DS} modulation occurs, we make use of (7) with equilibrium transmission spectra. By doing so, since $TS(E, V_{DS})$ depends on V_{DS}, we commit an error. Nevertheless, we can rapidly estimate whether a I_{DS} modulation occurs from equilibrium calculations that require much shorter computational times than nonequilibrium ones. The error is small and close to equilibrium. Thus, we use $\Delta \int TS$ as a simple and fast figure of merit for a first-order characterization of the sensor.

H. Computational Methods

We perform the calculations in QuantumATK (v. Q-2019.12) [25], [26]. We build the Au–C$_{60}$–Au molecular dot starting from the C$_{60}$ relaxed geometry and by placing two symmetric gold FCC (111) 4×4 slab electrodes with 11 layers each at $2.4 \, \text{Å}$ of distance through the surface (cleave) tool. The geometry is optimized with the reactive force field calculator (maximum force 0.05 eV/Å, LBFGS algorithm) [27], [28]. We obtain a total atom displacement of 4%, in agreement with theoretical and experimental results—total deformation less than 10% [18], [19], and we choose to neglect it in next calculations. We use EHT [29], with Hoffmann parameters; only for Ar, the Muller basis

set is used since no Hoffmann pseudopotential is available. We use the NEGF for the evaluation of TS and I_{DS} [20], [30], and we self-consistently solve the transport equations (NEGF) and the system electrostatics (Poisson's equation with a conjugate gradient solver), considering a convergence tolerance of 10^{-5} over the Hamiltonian variable (Pulay's mixing scheme). We consider a single-cell device, representing the single-molecule quantum dot, and we enforce periodic boundary conditions (PBCs) in the transverse direction x, and Dirichlet's boundary conditions in the transport direction z and in the transverse direction y—the latter to avoid artifacts related to PBC in the direction in which the gas molecules are placed. The enforced boundary conditions permit the simulation of a structure with crystalline gold electrodes, wide and shallow gold leads, and a single-molecule C_{60} channel. We consider always room temperature: 300 K; k-space sampling density [7, 7, 150] with Monkhorst–Pack–Grid, eventually increased on nonconvergence at [12, 12, 175]; energy cutoff at 75 hartree; self-energy calculator: Recursion.

III. RESULTS AND DISCUSSION

A. Effect of NO at Equilibrium and Transport Mechanism

We use nitric oxide (NO) as a case study. Fig. 3 reports the PDOS and the TS for the isolated Au–C_{60} dot (a), and in the presence of NO (b). As described in Section II-B, the C_{60} level at 0.79 eV (solid black line) is shifted at 0.77 eV and broadened (blue peak in the PDOS), while the degenerate peaks at -0.8 eV are shifted outside the considered energy range. We relate the origin of the PDOS states around Fermi energy (0 eV) to the mixing with S and D states. Indeed, this portion of the PDOS well matches the S/D contact PDOS, reported in Fig. S1. The TS well resembles the PDOS, with several TS peaks aligned with PDOS peaks. This highlights that the transmission from S to D is possible by tunneling through the molecular channel electron states. Interestingly, the effect of NO is to introduce a localized PDOS peak close to Fermi energy [see Fig. 3(b)]. The isolated NO level (dashed vertical line) significantly increases the PDOS at 0.045 eV (blue peak); nevertheless, TS is decreased around that energy as an effect of localization. Furthermore, NO enhances the presence of additional PDOS localized peaks [dashed arrows in Fig. 3(b)] with a consequent overall decrease of TS.

We estimate γ as the width at half height of the TS/PDOS peaks in Fig. 3. Then, through (1), we find a lifetime of the order of the femtosecond, meaning that on average every (few) fs, an electron pass from/to the S/D to/from the C_{60}. Literature data on C_{60} thermal vibration frequencies report vibrational periods of the order of $20 \div 120$ fs [31]. Therefore, since the transit time is tens or hundred times smaller, incoherent processes are confirmed to be negligible in the system under study. Indeed, from the standpoint of the electrons, the system is unperturbed during the S-to-D transmission (no scatterers are present in the channel). Moreover, from the considered timescales, we expect a deviation lesser than 10% over the total current when incoherent processes are considered.
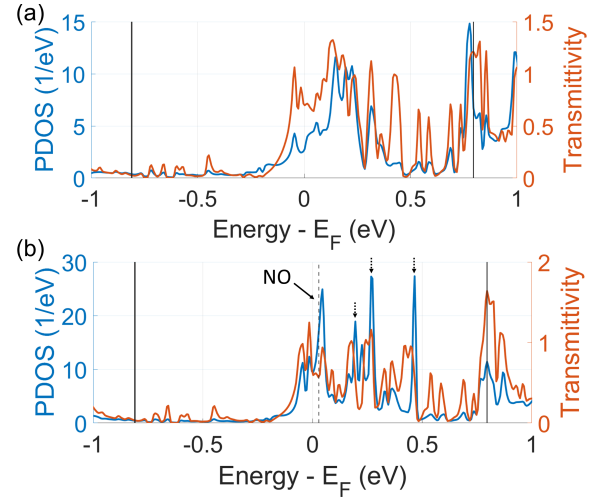

Fig. 3. Equilibrium PDOS (blue) onto the (a) C_{60} molecular channel and (b) C_{60} + NO when present NO, and relative TS (orange); the solid vertical black lines are the isolated C_{60} energy level (at left side degeneracy occurs), the dashed vertical lines are the isolated NO molecule energy level in the considered energy range.

B. Equilibrium TS and Effect of V_{DS}

Fig. 4(a) reports again the equilibrium TS with and without NO, while Fig. 4(b) reports the corresponding $\Delta \int TS$ in modulus. The small TS variations close to Fermi energy (0 eV)—solid arrow—produce small $\Delta \int TS$ deviation from zero for small BW values. The major effect of NO is to affect the circled TS peak, leading to the circled $\Delta \int TS$ peak. By further increasing the BW, the TS peaks highlighted with dashed arrows produce corresponding $\Delta \int TS$ modifications. From this equilibrium analysis, we expect a significant G and I_{DS} variation for BW = 0.5 eV ($V_{DS} = 0.5$ V). Nevertheless, the effect of increasing V_{DS} values is to modify and shift the circled TS peak in Fig. 4(a) toward higher E—see Fig. 4(c) red circles. Consequently, the modulated TS peak is included in the BW only for $V_{DS} = 1$ V, that is, it is in between E_{FD} and E_{FS}. Fig. 4(d) shows the effect of V_{DS} on the Au–C_{60} TS (without NO) and highlights the TS shift toward upper E.

C. Effect of NO in Nonequilibrium

Fig. 5(a) reports the TS at $V_{DS} = 1$ V, with and without NO. The main effect of NO is to reduce a TS peak, indicated with (A) and black arrows, from 1.585 to 0.8, and also to shift it in energy from 0.36 eV to 0.4 eV. Table I reports the (A) peak TS values, and the TE transmission coefficients composing it, with and without NO. Without NO, there are two main TEs contributing to the peak (A), with transmission coefficients 0.924 and 0.646, while the remaining TEs contribute to the TS peak with only 0.015 transmission probability. In the presence of NO, both TE_1 and TE_2 are reduced, with TE_2 extremely less transmitting. Fig. 5(c) and (d) reports the space projections of the TE_1 without and with NO, respectively. If NO is present, the TE surface lobes are reduced and less merged. Moreover, new TE lobes appear around NO, indicating that it plays a role in the electron transmission from S to D. In other words, the transmission occurs with different probability and in different space regions when NO is present. This is more marked by considering
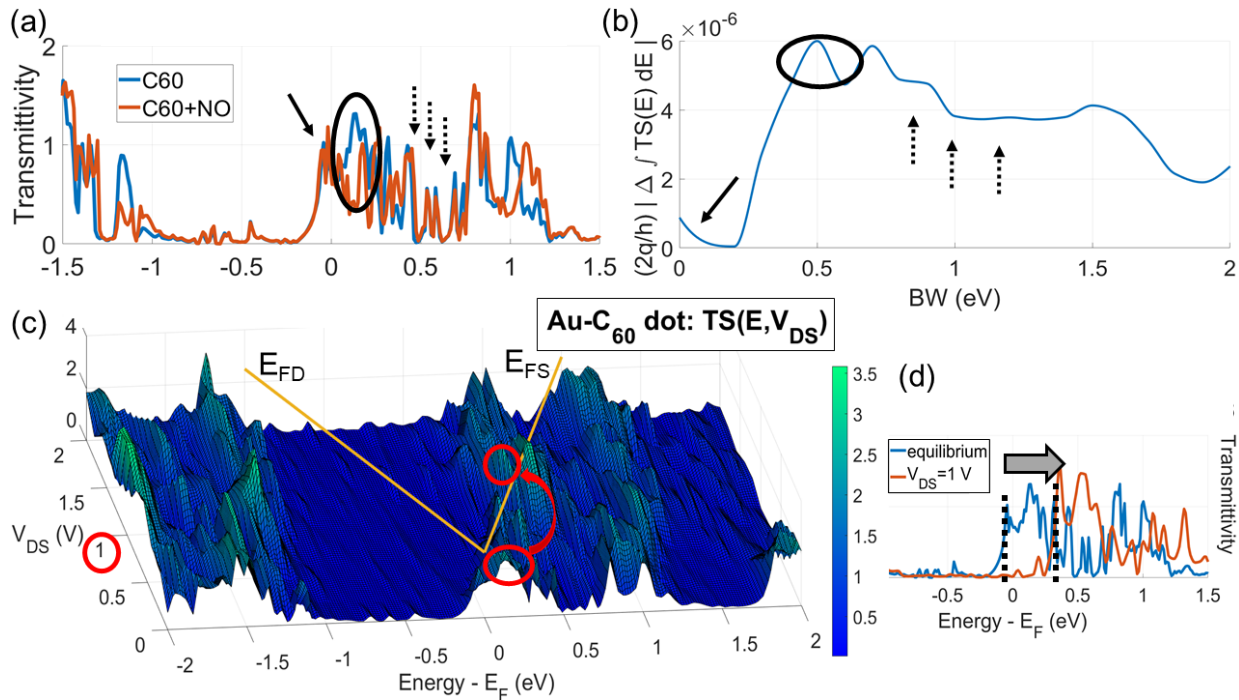
Fig. 4.   (a) Equilibrium *TS* w/o and with NO. (b) $(2q/h)|\Delta \int TS|$ referred *TS* in (a). (c) *TS*(E, V_{DS}) with NO, the yellow lines represent the S and D Fermi levels, the *TS* peak of interest is shifted at higher E and enters the BW at 1 V, as indicated by the red circles. (d) Au–C₆₀ *TS* at equilibrium and at 1 V.
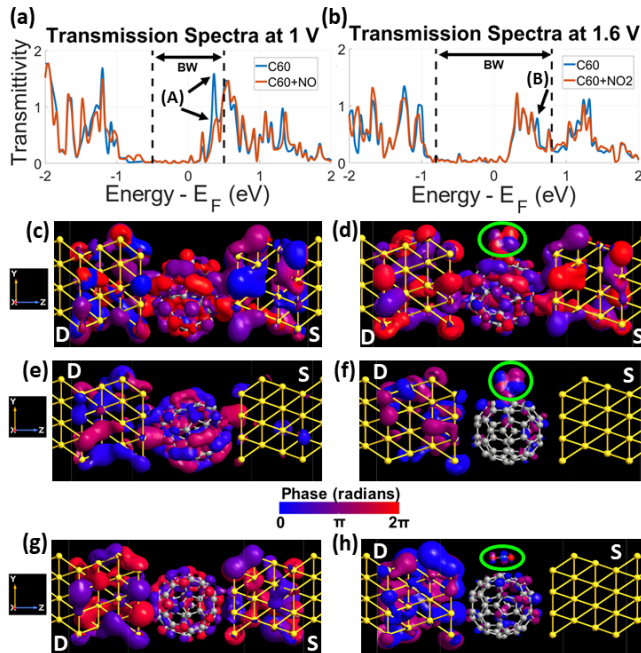

Fig. 5.   (a) and (b) *TS* of interest for NO and NO₂ detection. (c) and (d) TE₁ of peak (A) without and with NO, respectively. (e) and (f) TE₂ of peak (A) without and with NO, respectively. (f) and (g) TE₁ of peak (B) without and with NO, respectively. TE's isovalue is 0.175.

the TE₂ space projections—Fig. 5(e) and (f). No TE₂ surface envelopes the S contact while there are lobes around D. Therefore, at the considered iso-probability value (i.e., 0.175), there is a negligible S-to-C₆₀ transmission, while, if an electron is transmitted from S to C₆₀, then it can proceed toward the D. By comparison of Fig. 5(e) with Fig. 5(f), the total effect of NO is again to reduce the TE lobes and the relative

TABLE I
TS PEAKS AT 1 V AND RELATIVE TE VALUES [SEE FIG. 5(a)]

	TS peak (A)	TE₁	TE₂	remaining TEs
C₆₀	1.585	0.924	0.646	0.015
C₆₀+NO	0.8	0.735	0.006	0.059

transmission coefficient, especially at the S side, as indicated by the absence of TE₂ lobes in the S electrode.

This is in agreement with the more localized nature of the PDOS of Fig. 3 in the presence of NO.

Table II reports the Mulliken population analysis of the carbon atoms that are closest to NO. We focus on the valence electrons since the core ones' result is unperturbed. Notice that a positive/negative difference in Table II indicates a decrease/increase in electron probability density nearby the atom due to the target presence. In the presence of NO, there is a significant Mulliken population decrease in the carbon atoms close to oxygen, while an increase occurs in the carbon atoms nearby the nitrogen. Variations in the other carbon atoms are small compared to the ones already mentioned. The total variation of electron population in the C₆₀ is far below the unity, and on average there are 0.092 fewer electrons in the C₆₀ if NO is present, meaning that NO neither provokes a reduction nor oxidation of the C₆₀ channel.

From the TEs and Mulliken analyses, we conclude that NO produces a spatial electron wave function rearrangement in C₆₀ that results in a modification of the main TEs, that in turn leads to significant TS, G, and I_{DS} variations, according to what presented in Section II.

D. Effect of Other Targets

Fig. S2 reports the PDOS and the TS with and without NO₂. Similar to NO, also NO₂ introduces localized states close to Fermi energy, even if TS results globally less affected

TABLE II
MULLIKEN POPULATION OF VALENCE SHELLS OF A SUBSET OF C_{60} CARBON ATOMS (CORE SHELLS ARE UNPERTURBED)

C atom identifier	C_{60} only (1 V)	C_{60}+NO (1 V)	difference
75 (nearby O)	4.023	4.021	+0.002
84 (nearby O)	3.999	4.014	-0.015
93 (nearby O)	4.010	3.92	+0.090
99 (nearby O)	4.004	3.95	+0.054
102 (nearby N)	4.000	4.020	-0.020
108 (nearby N)	4.004	4.018	-0.014
111 (nearby N)	3.997	3.996	+0.001
117 (nearby N)	4.009	4.015	-0.006
C atom identifier	C_{60} only (1.6 V)	C_{60}+NO_2 (1.6 V)	difference
75 (nearby O)	4.026	4.022	+0.004
84 (nearby O)	4.008	3.994	+0.014
93 (nearby O)	4.006	3.95	+0.056
99 (nearby O)	4.003	3.957	+0.046
108 (nearby O)	4.007	3.993	+0.014
102 (nearby N)	4.008	4.059	-0.051
111 (nearby N)	3.998	3.997	+0.001
117 (nearby N)	4.006	4.014	-0.008
C atom identifier	C_{60} only (1.4 V)	C_{60}+CH_4 (1.4 V)	difference
75 (nearby CH_4)	4.025	4.023	+0.002
78 (nearby CH_4)	4.011	4.013	-0.002
84 (nearby CH_4)	4.006	4.015	-0.009
87 (nearby CH_4)	4.003	4.003	0
93 (nearby CH_4)	4.006	3.987	+0.019
99 (nearby CH_4)	4.003	4.009	-0.006
102 (nearby CH_4)	4.007	4.015	-0.008
108 (nearby CH_4)	4.006	4.006	0
111 (nearby CH_4)	3.999	3.997	+0.002
117 (nearby CH_4)	4.006	4.009	-0.003

Fig. 6. (a) TE_1 of the main TS peak within the BW at 1.4 V. (b) TE_1 in the presence of CH_4, the isovalue is 0.07.

Fig. 7. Au–C_{60} $I_{DS}(V_{DS})$ curve; simulation data and their cubic spline interpolation are reported. Inset shows the equilibrium TS.

by NO_2 than by NO. Moreover, and by proceeding as done in Section III-B, we expect that NO_2 significantly modulates TS at 1.6 V, as reported in Fig. 5(b)—black arrow. As the main effect, the transmission peak (B) disappears when NO_2 is present. The reason is related again to a space modification of the transmission channel, as confirmed in Fig. 5(g) and (h), in which the TE_1 lobes are reduced by the presence of NO_2. Again, from the Mulliken analysis in Table II, we find that the total variation of electron population in C_{60} is 0.076 less electrons if NO_2 is present. This proves that extra electrons are neither added nor removed from the C_{60} dot, and the sensing mechanism is analogous to the NO one.

Similar results can be obtained with NH_3 even if we do not report them here for brevity. Instead, we focus on the case of CH_4, in which the analysis of the main TE (see Fig. 6) shows no relevant TE modulation if CH_4 is present. Furthermore, CH_4 is not enveloped by the TE surface, meaning that it does not significantly affect the main TE transmission channel. The only difference is a constant phase difference with CH_4 [colors in Fig. 6(a) and (b)]. The Mulliken analysis (see Table II) shows that there are only 0.005 extra electrons with CH_4. Such difference is 18.4 times smaller than with NO and 15.2 times smaller than with NO_2, indicating much less electron cloud rearrangement.

E. Bias-Dependent Response

Sections III-C and III-D show that if a target is able to induce a significant electron rearrangement in the Au–C_{60} dot, a significant TE spatial modulation occurs, implying a TS modulation at a specific E. Fig. 5 highlights that TS is modulated only at some E. This induces a voltage dependency
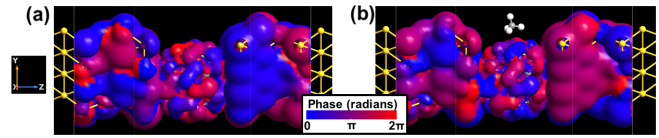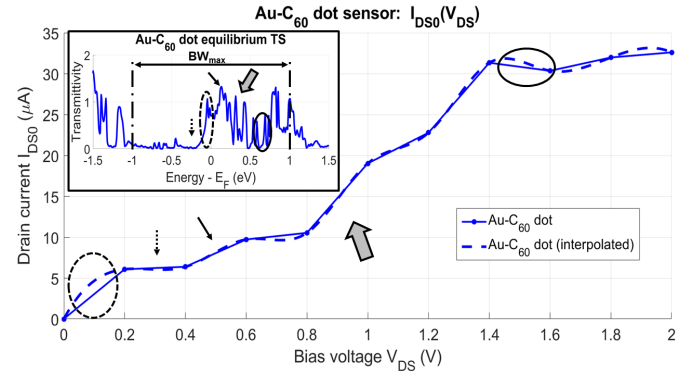
of the sensor response, as we discussed in Section II-E. Indeed, a modification of $TS(E)$ can produce an effect on G and I_{DS} only if the energy E at which the modification occurs is included or close the BW, thus originating a V_{DS}-dependent ΔI_{DS}. The voltage-dependent response is an advantage: if a sensor presents a selective response to different targets at different V_{DS}, by changing the V_{DS}, the sensor can detect the various targets.

The voltage-dependent response is in contrast to conventional MOX-based nanosensors, in which G is modulated through free carrier concentration modulation caused by surface oxidation/reduction processes [3]. The origin of this discrepancy is in the different transport mechanisms. Conventional MOX devices rely on semiclassical transport, governed by ohmic conductance, with G modulated through free carrier concentration modulation. The Au–C_{60} dot relies on ballistic transport, governed by Landauer's equation, with G proportional to the $TS(E)$ integral in E.

F. Current Modulation and Amperometric Sensing

Fig. 7 reports the $I_{DS}(V_{DS})$ characteristic of the Au–C_{60} molecular dot, which is in agreement with the experimental results reported in [13]. The equilibrium Au–C_{60} TS, reported in the inset of Fig. 7, is enough to intuitively explain the $I_{DS}(V_{DS})$ curve. For small BW (dashed circle), a sharp TS peak is already conducting, leading to the sharp increase of I_{DS} up to 0.2 V. Then the absence of transmitting states below the Fermi energy (dashed arrow) causes the first plateau in I_{DS}. For increasing BW, the TS peaks indicated with the solid arrow first and then with the gray arrow, induce the corresponding increase of I_{DS}. A second plateau (solid circle) occurs when small TS peaks enter the BW, producing a small effect on I_{DS}.

Fig. 8 reports the ΔI_{DS}, calculated as in (4), for different targets and common atmospheric gases. Even if current modulations occur with all targets, they are very small in the case of CH_4 and C_4H_{10} [see Fig. 8(a)], where the maximum ΔI_{DS}
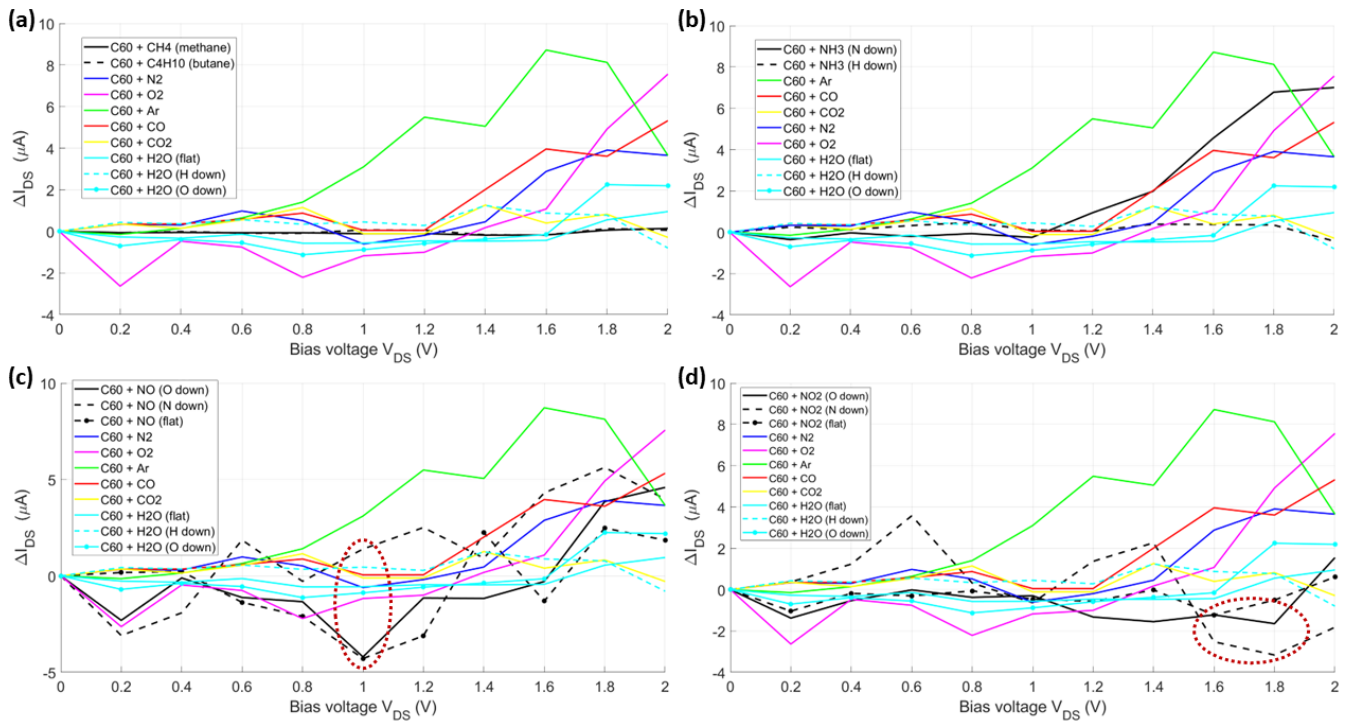
Fig. 8. ΔI_{DS} with different analytes and atmospheric gases. Various orientations are considered for polar molecules ("down" indicates the element of the target molecule that is closest to Au–C$_{60}$ dot; "flat" if all are equidistant). Targets: (a) CH$_4$ and C$_4$H$_{10}$; (b) NH$_3$; (c) NO$_2$; and (d) NO.

is slightly below 180 nA at 1.5 V. We relate such small ΔI_{DS} to the unperturbed TE and small electron rearrangement in the Mulliken population discussed in Section III-D. Also the selectivity is poor: the responses to common atmospheric gases like water (O "down") and O$_2$ are too similar to the CH$_4$ and C$_4$H$_{10}$ ones, with only 22 nA of margin at 1.6 V. Thus, the detection of CH$_4$ and C$_4$H$_{10}$ in air is difficult.

In the case of ammonia [see Fig. 8(b)], larger ΔI_{DS} are obtained, with values in between 111 and 470 nA, reaching also 6.78 and 7 μA at high bias (1.8 and 2 V) for the "N down" orientation. Even if NH$_3$ detection is possible in terms of sensitivity, the selectivity in the air does not permit reliable detection in the presence of common atmospheric gases, since no reliable ΔI_{DS} margins are obtained.

The Au–C$_{60}$ dot results instead able to reliably detect both NO$_2$ and NO (see Fig. 8(c) and (d)—dashed circles). In particular, for NO$_2$ and V_{DS} between 1.6 and 1.8 V, the obtained ΔI_{DS} with all the NO$_2$ orientations are effective, with 1.22 μA of deviation w.r.t. $I_{DS,0}$, and with 0.79 μA of margin from the current with water ("flat"). Moreover, the effect of NO$_2$ (all orientations) is to decrease I_{DS} more than any other gas. Therefore, a reliable operating V_{DS} can be 1.6 V. Similar considerations hold for NO at 1 V. Two NO orientations over three lead to 4.29 μA of current decrease w.r.t. $I_{DS,0}$, with a margin of 3.11 μA with the O$_2$ curve. Anyway, the NO orientation "N down" increases the current (positive ΔI_{DS}). Even if this would likely complicate the front-end electronics, that should correctly handle it, the detection is reliably possible. Indeed, the current obtained with NO ("N down") has 0.94 and 1.7 μA of margin with the curves with water ("H down") and Ar. The ΔI_{DS} obtained with NO

and NO$_2$ are about one order of magnitude greater than those with CH$_4$ and C$_4$H$_{10}$. We find the reason for the greater electron rearrangement and TE modification caused by NO and NO$_2$ (see Section III-C).

G. Sensing Reliability and Detection by Events

In this section, we address the sensing mechanism reliability in the air at room temperature. In general, more chemical species are present at the same time in the air. Nevertheless, by considering that at normal temperature (298.15 K) and pressure (1 bar) [32], one single molecule of those composing air occupies on average a volume of edge 3 ÷ 5 nm [1] and that the C$_{60}$ radius is around 0.7 nm with a gold nanogap of around 1 nm (between three and five times smaller than the average volume occupied by a single molecule in air), it is very likely that only one molecule interact with the Au–C$_{60}$ at a time, generating a defined event in terms of current modulation. Furthermore, Table S3 reports the C$_{60}$–target interaction energies. The obtained values show that for all the considered targets and common atmospheric compounds, there is no adsorption of the species on C$_{60}$, since no target–C$_{60}$ stability is achieved, at least for the considered relative orientation and exposed face of C$_{60}$. Consequently, the sensing mechanism is purely physical with a gas molecule approaching the Au–C$_{60}$ sensor, producing a current modulation through interaction and a TS modulation, and bouncing away because of the scattering with the sensor itself. During an event, the target can interact with the lateral sides of the C$_{60}$, close to S and D, instead of with the central portion of C$_{60}$. We consider it in Fig. 9(a) and (b) that report the results in the case of NO and NO$_2$, respectively. When NO interacts with lateral sides of
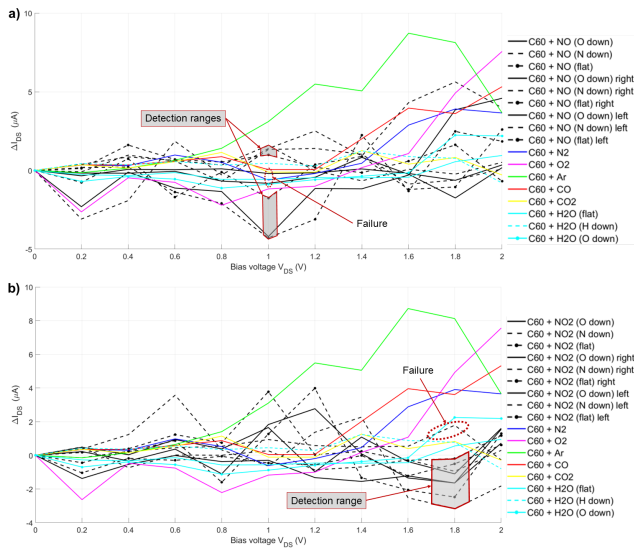
Fig. 9. (a) NO_2 detection range and failure case and (b) NO detection ranges and failure case when the NO_2 and NO molecules are interacting with side parts of the sensor. In the legend, we do not make a distinction among the interaction regions but only about the target orientations.

C_{60}, its detection is still possible in seven over nine possible cases (three target orientations per position: centered on C_{60} or close to S/D). In particular, we find two ranges (gray regions) in which selective detection is possible at 1 V, while in two over nine cases a selectivity failure occurs, since the current is too close to values obtained with common atmospheric compounds. Also in the case of NO_2, we find a possible detection range, including eight over nine total cases, while in one case a selectivity failure occurs.

We postpone to future works the detailed analysis of the dynamic behavior of the sensor and its reliability features. Nevertheless, we interpret the preliminary results of this section as promising for performing target detection by events, in which a single event can be detected with a given error probability and the target concentration can be extrapolated by statistical analysis of such events, with the advantage of a nonnecessary sensor regeneration after each sensing event.

H. Process Variations

The purpose of this section is to understand whether some of the most common fabrication nonidealities can compromise or even nullify the effect of targets on the final sensor response.

First of all, a larger gold nanogap might be created, mismatching the C_{60}–contact distance. We thus consider additional contact–C_{60} distances: 2.7, 3, 3.3, and 3.6 Å. We interpolate the I_{DS} curves w.r.t. C_{60}–contact distance— Fig. 10(a)—and we find a good exponential trend for all V_{DS}. Fig. 10(b)–(e) reports the highest occupied MPSH—that is, electron orbital—for different distances. By increasing the distance, there are gradually more evident barriers. This agrees with the experimental result in [33], in which different contact distances are forced and the creation of a chemical bond results gradually, from physisorption to chemisorption. The MPSH analysis explains the exponential decrease of I_{DS} with
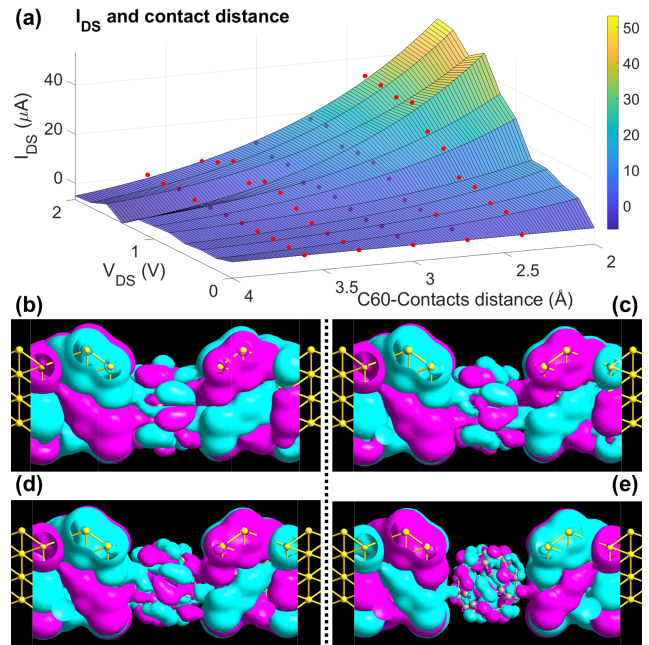

Fig. 10. (a) I_{DS} exponential interpolation—simulated data are the red dots. (b)–(e) MPSH with contact–C_{60} distance of 2.4 Å, 2.7 Å, 3 Å, and 3.6 Å, respectively. Colors represent the orbital phase.

TABLE III
ΔI_{DS} AT DIFFERENT CONTACT DISTANCES AND C_{60} ORIENTATIONS

	Absolute	current	variations	ΔI_{DS}	(μA)	
Orient.	Analyte	2.4 Å	2.7 Å	3 Å	3.3 Å	3.6 Å
Fig. 1(b)	NO	1.740	1.386	0.809	3.425	0.271
Fig. 1(b)	NO_2	0.452	1.067	0.664	3.125	0.199
Fig. 1(d)	NO	1.464	1.151	1.378	0.384	0.297
Fig. 1(d)	NO_2	1.436	0.857	0.678	0.297	0.212
	Percentage	current	variations	$\Delta I_{DS\%}$	(%)	
Orient.	Analyte	2.4 Å	2.7 Å	3 Å	3.3 Å	3.6 Å
Fig. 1(b)	NO	10.15	24.74	38.36	74.11	152.81
Fig. 1(b)	NO_2	3.61	15.18	32.54	72.71	66.49
Fig. 1(d)	NO	15.99	43.55	54.71	57.36	273.49
Fig. 1(d)	NO_2	13.37	17.84	31.18	45.58	72.69

contact–C_{60} distance. Indeed, tunneling current exponentially decreases with barrier width [20], and Fig. 10(b)–(e) shows the presence of increasing width barriers with increasing contact– C_{60} distance. Moreover, Fig. 10(b) confirms the Au–C_{60} covalent chemical bond at a distance of 2.4 Å. Table III reports the ΔI_{DS} and $\Delta I_{DS\%}$ values obtained with NO and NO_2 for different contact-C_{60} distances. The ΔI_{DS} values decrease with distance due to wider barriers and I_{DS} decrease. Whereas $\Delta I_{DS\%}$ values increase. Even if lower ΔI_{DS} are more difficult to be detectable, greater $\Delta I_{DS\%}$ variations are an advantage, since the sensor presents increased relative sensibility to targets.

In addition, competitor chemical/physical processes can affect the C_{60} anchoring, that might be rotated, as in Fig. 1(c)—corresponding to the case investigated in [9]. We find no disadvantage (neither advantage) in this case, both in terms of ΔI_{DS} and $\Delta I_{DS\%}$—Table III. We believe that the theoretical results of this section can be useful in support of future experimental investigations of the theorized Au–C_{60} sensor.

IV. Conclusion

We investigated the Au–C_{60} molecular dot as a novel single-molecule gas sensor. From our results, the Au–C_{60} dot is promising for selectively performing amperometric detection of NO at 1 V and NO_2 in the range 1.6 V ÷ 1.8 V, with detectable current deviations at room temperature (300 K) in the range 1 μA ÷ 4.3 μA. The current modulation capability by target presence makes the proposed sensor appealing for automatic real-time environmental monitoring of chemical species. The sensor also presents good sensitivity to NH_3 but poor selectivity in air, and poor response to CH_4 and C_4H_{10}. Additionally, we provided insights into the sensing mechanism, showing that the targets produce a space rearrangement of electron population with consequent modulation of the sensor TEs, that in turn causes the G and I_{DS} modulation. We relate the energy-dependent modulation of TS to the peculiar voltage-dependent sensor response, which we believe can be used to perform multipurpose amperometric sensing by suitably tuning V_{DS} at which the sensor selectively reacts to specific targets.

From the preliminary results, we obtained concerning the sensing mechanism reliability in air, the sensor is promising for detection based on single events of interaction with gas molecules, with the advantage of requiring no sensor regeneration after the sensing event. Finally, from the considered fabrication nonideality results, no significant performance degradation is found, making the device appealing for future experimental verifications.

We believe our results to motivate future investigations in this field, especially concerning the sensor–target dynamic interactions, toward performance-oriented device engineering, and concerning experimental works.

References

[1] R. McIlveen, *Fundamentals of Weather and Climate*. Oxford, U.K.: Oxford Univ. Press, 2010.

[2] W. H. O. R. O. for Europe, *Review of Evidence on Health Aspects of Air Pollution—REVIHAAP Project: Final Technical Report*, World Health Organization, Geneva, Switzerland, 2013. Accessed: 2021. [Online]. Available: https://www.who.int/news-room/fact-sheets/detail/ambient-(outdoor)-air-quality-and-health

[3] K. Wetchakun *et al.*, "Semiconducting metal oxides as sensors for environmentally hazardous gases," *Sens. Actuators B, Chem.*, vol. 160, no. 1, pp. 580–591, 2011.

[4] N. Kaur, M. Singh, and E. Comini, "One-dimensional nanostructured oxide chemoresistive sensors," *Langmuir*, vol. 36, no. 23, pp. 6326–6344, 2020.

[5] J. J. Gooding, "The exciting world of single molecule sensors," *ACS Sensors*, vol. 1, no. 10, pp. 1163–1164, 2016.

[6] J. J. Gooding and K. Gaus, "Single-molecule sensors: Challenges and opportunities for quantitative analysis," *Angew. Chem. Int. Ed.*, vol. 55, no. 38, pp. 11354–11366, 2016.

[7] Y. Li, C. Yang, and X. Guo, "Single-molecule electrical detection: A promising route toward the fundamental limits of chemistry and life science," *Accounts Chem. Res.*, vol. 53, no. 1, pp. 159–169, Jan. 2020.

[8] K. Sattler, *Handbook of Nanophysics, Clusters and Fullerenes*. Boca Raton, FL, USA: CRC Press, 2010.

[9] A. Nasri, A. Boubaker, B. Hafsi, W. Khaldi, and A. Kalboussi, "High-sensitivity sensor using C_{60}-single molecule transistor," *IEEE Sensors J.*, vol. 18, no. 1, pp. 248–254, Jan. 2018.

[10] S. Pilehvar and K. De Wael, "Recent advances in electrochemical biosensors based on fullerene-C_{60} nano-structured platforms," *Biosensors*, vol. 5, no. 4, pp. 712–735, Nov. 2015.

[11] J. A. Rather and K. De Wael, "Fullerene-C_{60} sensor for ultra-high sensitive detection of bisphenol–A and its treatment by green technology," *Sens. Actuators B, Chem.*, vol. 176, pp. 110–117, Jan. 2013.

[12] B. Hammer and J. K. Norskov, "Why gold is the noblest of all the metals," *Nature*, vol. 376, no. 6537, pp. 238–240, Jul. 1995.

[13] T. Böhler, J. Grebing, A. Mayer-Gindner, H. V. Löhneysen, and E. Scheer, "Mechanically controllable break-junctions for use as electrodes for molecular electronics," *Nanotechnology*, vol. 15, no. 7, pp. S465–S471, May 2004.

[14] I. Rattalino, P. Motto, G. Piccinini, and D. Demarchi, "A new validation method for modeling nanogap fabrication by electromigration, based on the resistance–voltage (R–V) curve analysis," *Phys. Lett. A*, vol. 376, no. 30, pp. 2134–2140, 2012.

[15] D. Demarchi, P. Civera, G. Piccinini, M. Cocuzza, and D. Perrone, "Electrothermal modelling for EIBJ nanogap fabrication," *Electrochim. Acta*, vol. 54, no. 25, pp. 6003–6009, Oct. 2009.

[16] V. Dubois *et al.*, "Massively parallel fabrication of crack-defined gold break junctions featuring sub-3 nm gaps for molecular devices," *Nature Commun.*, vol. 9, no. 1, p. 3433, 2018.

[17] D. Xiang *et al.*, "Three-terminal single-molecule junctions formed by mechanically controllable break junctions with side gating," *Nano Lett.*, vol. 13, no. 6, pp. 2809–2813, Jun. 2013.

[18] R. J. Maurer *et al.*, "Adsorption structures and energetics of molecules on metal surfaces: Bridging experiment and theory," *Prog. Surf. Sci.*, vol. 91, no. 2, pp. 72–100, May 2016.

[19] H. Shin *et al.*, "Structure and dynamics of C_{60} molecules on Au(111)," *Phys. Rev. B, Condens. Matter*, vol. 89, Jun. 2014, Art. no. 245428.

[20] S. Datta, *Quantum Transport: Atom to Transistor*. Cambridge, U.K.: Cambridge Univ. Press, 2005.

[21] S. Datta, *Electronic Transport in Mesoscopic Systems*. Cambridge, U.K.: Cambridge Univ. Press, 1995.

[22] S. Karthäuser, "Control of molecule-based transport for future molecular devices," *J. Phys., Condens. Matter*, vol. 23, no. 1, Nov. 2010, Art. no. 013001.

[23] F. London, "The general theory of molecular forces," *Trans. Faraday Soc.*, vol. 33, p. 8b–26, Jan. 1937.

[24] M. Waller and S. Grimme, *Weak Intermolecular Interactions: A Supermolecular Approach*. Amsterdam, The Netherlands: Springer 2016.

[25] S. Smidstrup *et al.*, "QuantumATK: An integrated platform of electronic and atomic-scale modelling tools," *J. Phys., Condens. Matter*, vol. 32, no. 1, Jan. 2020, Art. no. 015901.

[26] *QuantumATK Version Q-2019.12, Synopsys QuantumATK*. Accessed: Sep. 10, 2022. [Online]. Available: https://www.synopsys.com/silicon/quantumatk.html

[27] A. C. T. van Duin, S. Dasgupta, F. Lorant, and W. A. Goddard, "ReaxFF: A reactive force field for hydrocarbons," *J. Phys. Chem. A*, vol. 105, no. 41, pp. 9396–9409, 2001.

[28] T. T. Järvi, A. C. T. van Duin, K. Nordlund, and W. A. Goddard, "Development of interatomic reaxff potentials for Au–S–C–H systems," *J. Phys. Chem. A*, vol. 115, no. 37, pp. 10315–10322, 2011.

[29] K. Stokbro, D. E. Petersen, S. Smidstrup, A. Blom, M. Ipsen, and K. Kaasbjerg, "Semiempirical model for nanoscale device simulations," *Phys. Rev. B, Condens. Matter*, vol. 82, no. 7, Aug. 2010, Art. no. 075420.

[30] M. Brandbyge, J.-L. Mozos, P. Ordejón, J. Taylor, and K. Stokbro, "Density-functional method for nonequilibrium electron transport," *Phys. Rev. B, Condens. Matter*, vol. 65, no. 16, Mar. 2002, Art. no. 165401.

[31] D. Jing and Z. Pan, "Molecular vibrational modes of C_{60} and C_{70} via finite element method," *Eur. J. Mech.-A/Solids*, vol. 28, no. 5, pp. 948–954, Sep. 2009.

[32] T. Doiron. (2007). *20 Degrees Celsius—A Short History of the Standard Reference Temperature for Industrial Dimensional Measurements*. Accessed: Jan. 1, 2007. [Online]. Available: https://tsapps.nist.gov/publication/get_pdf.cfm?pub_id=823211

[33] F. Huber, J. Berwanger, S. Polesya, S. Mankovsky, H. Ebert, and F. J. Giessibl, "Chemical bond formation showing a transition from physisorption to chemisorption," *Science*, vol. 366, no. 6462, pp. 235–238, Oct. 2019.